Carbon 168 (2020) 701–709

Contents lists available at ScienceDirect

Carbon

journal homepage: www.elsevier.com/locate/carbon

Three-dimensional nitrogen doped hierarchically porous carbon aerogels with ultrahigh specific surface area for high-performance supercapacitors and flexible micro-supercapacitors

Yunfang Gao [a, 1], Shuanghao Zheng [b, d, 1], Hanli Fu [a], Jiaxin Ma [b, c, d], Xin Xu [a], Li Guan [a], Haihua Wu [a, *], Zhong-Shuai Wu [b, d, **]

[a] State Key Laboratory Breeding Base of Green-Chemical Synthesis Technology, College of Chemical Engineering, Zhejiang University of Technology, 18 Chaowang Rd, Hangzhou, 310014, China
[b] State Key Laboratory of Catalysis, Dalian Institute of Chemical Physics, Chinese Academy of Sciences, 457 Zhongshan Road, Dalian, 116023, China
[c] Dalian National Laboratory for Clean Energy, Chinese Academy of Sciences, 457 Zhongshan Road, Dalian, 116023, China
[d] University of Chinese Academy of Sciences, 19 A Yuquan Rd, Shijingshan District, Beijing, 100049, China

ARTICLE INFO

Article history:
Received 25 April 2020
Received in revised form
19 June 2020
Accepted 21 June 2020
Available online 15 July 2020

Keywords:
Carbon aerogel
Nitrogen doped
Supercapacitors
Micro-supercapacitors
Energy storage

ABSTRACT

Rational design of electrode materials with tunable pore structure and large specific surface area (SSA) are of great importance for boosting high-performance supercapacitors (SCs) and micro-supercapacitors (MSCs). Here we develop a nitrogen doped hierarchically porous carbon aerogel (NPCA) derived from chitosan biomass *via* a combined chelation reaction and freeze-drying procedures for SCs and MSCs. The NPCA exhibits three-dimensional (3D) reticular texture with ultrahigh SSA of 2529 $m^2\ g^{-1}$, which is highly responsible for accommodating large charge storage. The interconnected micro-/mesopores distributed on the continuous carbon network can create more adsorption sites and commodious channels for fast ion diffusion, yet offer high electrical conductivity for rapid electron transport. As a result, the assembled symmetric SC using NPCA exhibits enhanced electrochemical performance with energy density of 6.8 Wh kg^{-1} at power density of 251 W kg^{-1}. More importantly, the solid-state flexible NPCA-MSC presents high areal capacitance of 25.6 mF cm^{-2}, outstanding energy density of 0.78 μWh cm^{-2}, exceptional cyclability with only 1% capacitance fading after 10000 cycles, and superior flexibility with capacitance retention of 99%. Therefore, this biomass-derived carbon strategy will provide numerous opportunities to develop low-cost 3D micro-/mesoporous heteroatom-doped carbon aerogels for high-performance SCs and MSCs in a large scale.

1. Introduction

The ampliative need for electric vehicles, portable equipment and smart grids has forcefully stimulated the rapid development of electrochemical energy storage devices with high permanence, large energy density and cost efficiency, including supercapacitors (SCs) and batteries [1–3]. Different from batteries, SCs convert electrical and chemical energies *via* electrical double-layer capacitance or pseudocapacitance, characterizing high power density, fast rate response, long lifespan and wide operation temperature range, which are very promising candidates for next-generation stockpile equipment [4–7]. Except for large-scale energy sector, planar micro-supercapacitors (MSCs), as microscale electrochemical energy storage devices, featured by mechanical flexibility, miniaturization, lightweight and high safety, emerge as competitive alternatives to complement or replace micro-batteries for wearable and miniaturized electronics [8,9]. So far, considerable efforts have been devoted to constructing high-performance electrode materials for SCs and MSCs, such as transition metal oxides, conducting polymers and porous carbon [10,11]. However, transition metal oxides and conducting polymers for the SCs and MSCs, driven by faradaic redox reactions at the electrode/electrolyte interface, suffer from poor cyclability and rate capability, which

---

* Corresponding author.

** Corresponding author. State Key Laboratory of Catalysis, Dalian Institute of Chemical Physics, Chinese Academy of Sciences, 457 Zhongshan Road, Dalian, 116023, China.

E-mail addresses: haihuawu@zjut.edu.cn (H. Wu), wuzs@dicp.ac.cn (Z.-S. Wu).

[1] These authors have contributed equally to this work.

https://doi.org/10.1016/j.carbon.2020.06.063
0008-6223/© 2020 Elsevier Ltd. All rights reserved.

restricts their widely commercial application [12]. Alternatively, carbon materials, *e.g.*, activated carbon [13], carbon aerogels [14], carbon onions [15], carbon nanotubes [16], graphene [17] and carbon fibers [18], relying on fast electrostatic adsorption of electrolyte ions at the surface to store energy, have been regarded as the most attractive class of electrode materials for long-life and high-power SCs and MSCs. At present, research has been focused on improving the energy density and lowering the cost without scarifying the holistic electrochemical performance.

As is well known for ultralight materials, carbon aerogels have appealed intensive attentions toward high energy storage due to their large surface area, low mass density, high porosity (>80%) and outstanding electrical conductivity [19,20]. Moreover, the porous structure with three-dimensionally (3D) reticular network of carbon aerogels can provide easy access for the continuous migration of ion/molecules and rapid transportation of electrons, making carbon aerogels the ideal electrode materials for SCs. It is noted that the specific surface area (SSA) and pore structure are the vital parameters of electrode materials for electrical double-layer capacitors, which largely determine the specific capacitance and energy density [21]. For instance, Cheng et al. reported carbon fiber aerogels with various SSA ranging from 1536 to 2436 $m^2\ g^{-1}$ by tuning the amount of KOH during the activation process [22]. P. Hao et al. synthesized porous carbon aerogels with the co-existence of macro/meso/micropores, exhibiting SSA of 2000 $m^2\ g^{-1}$ [23]. Although the SSA can be enlarged by KOH activation, the intrinsic 3D network of carbon aerogels is vulnerable to destruction during the second-carbonization process and the pore structure is uncontrollable. In addition, it should be mentioned that micropores can provide more effective sites for energy storage, and small-sized mesopores are expected to maximize the capacitance by offering adequate path for fast ion diffusion [24–27].

In general, petroleum-based chemical products are employed as raw materials to prepare carbon materials, introducing the high price together with environmental pollution, which greatly limit their widely applications in market [28–30]. To this end, researchers have paid substantial attention on renewable and green biomass as carbon sources in consideration of their bioremediation, eco-friendliness and abundant storage. Chitosan, a biopolymer derived from N-deacetylation of chitin in fungus cytoderm, crustacean shell and insect exoskeleton, has been largely used in medicine and biology because of good medical properties and biocompatibility [31]. It is one of the most abundant biopolymers in nature, but its application in electrode materials for SCs/MSCs is still unexplored [32]. Chitosan is polymerized by N-acetylglucosamine monomers, and the active amino/hydroxyl groups enable it to chelate with metal ions and thus form a 3D reticular porous network with uniform pore structure, making it a potential alternative to prepare carbon aerogel with no need for activation process. Moreover, the plentiful nitrogen atoms in chitosan can fulfill a nitrogen self-doped procedure to obtain N-doped carbon aerogel for high performance SCs and MSCs, without the additional nitrogen precursor. Nevertheless, the design and fabrication of chitosan derived carbon aerogels with high surface area, large nitrogen content and controllable pore structure remain rarely reported for electrochemical capacitive energy storage.

Herein, we report a general cost-effective biomass strategy for the synthesis of nitrogen self-doped hierarchically porous carbon aerogel (NPCA) with 3D reticular architecture derived from chitosan using chelation reaction with Zn^{2+} without additional nitrogen source, followed by freeze-drying and carbonization. The original 3D network of Zn-chitosan complex can be well reserved under freeze-drying procedure. The as-synthesized NPCA presents extremely large SSA of 2529 $m^2\ g^{-1}$, and high nitrogen content of 7.42 wt%, associated with interconnected micropores and small-sized mesopores centering at ~3 nm. Benefiting from these advantages, the resulting NPCA electrode delivers excellent specific capacitance of 267 $F\ g^{-1}$ at current density of 1 $A\ g^{-1}$, and long-term cyclability with 100% capacitance retention after 10000 cycles in 6 M KOH electrolyte. The as-assembled symmetric SC based on NPCA shows large energy density of 6.8 $Wh\ kg^{-1}$ at power density of 251 $W\ kg^{-1}$. Furthermore, the resulting NPCA-based flexible MSC exhibits high capacitance of 25.6 $mF\ cm^{-2}$, exceptional areal energy density of 0.78 $\mu Wh\ cm^{-2}$, superior cycling stability with 99% capacitance retention after 10000 cycles, and outstanding flexibility. To the best of our knowledge, this is the first demonstration of carbon aerogels for MSCs.

2. Experimental

2.1. Materials preparation

All chemicals used in this work were purchased from Aladdin (Shanghai, China) without further purification. All aqueous solutions were prepared with ultrapure water of 18.2 MΩ (Milli-Q, Millipore).

3g chitosan was dissolved in 0.1 M 100 mL acetic acid and stirred for 30 min. 9 g zinc chloride was dissolved in 30 mL distilled water, and added to the above solution to form gelatinous Zn-chitosan complex, followed by freezing at −40 °C for 8 h and then drying at −60 °C for 48 h in a lyophilizer (Scientz-18ND, Scientz). The as-formed Zn-chitosan aerogel was carbonized at 800 °C for 2 h in N_2 gas and then the obtained sample was ground and leached in 0.1 M HCl solution to remove the remaining zinc ions. After that, the precipitate was washed with deionized water thoroughly until the filtrate became neutral. Finally, the obtained material was dried in a vacuum oven at 80 °C for 24 h and denoted as N-doped porous carbon aerogel (NPCA). For comparison, chitosan zinc complex derived porous carbon according to the same method, except substituting the freeze-drying process with directly drying at 100 °C, was prepared, and denoted as N-doped porous carbon (NPC). In addition, the carbon aerogel without the addition of zinc chloride solution was also synthesized, and denoted as CA.

2.2. Materials characterizations

The crystal structures of samples were determined using X-ray diffraction (XRD, D/max 1200, Cu Kα radiation, PANalytical, Netherland). The Raman spectra were measured on a Micro Raman Spectrometer (JOBIN YVON, Paris, France). Transmission electron microscopy (TEM, Tecnai G2 F20 U-TWIN), scanning electron microscopy (SEM) and energy-dispersive X-ray spectroscopy (EDX, Hitachi S4800) were employed to characterize the morphologies and elements of the samples. The SSA and pore structure were obtained from the N_2 adsorption/desorption isotherms at 77 K by an ASAP 2010 instrument (Micromeritics, USA). The surface composition and element state were collected by X-ray photoelectron spectroscopy (XPS, Kratos AXIS Ultra DLD).

2.3. Fabrication of solid-state NPCA-MSC

NPCA based micro-supercapacitor (NPCA-MSC) was assembled by the mask-assisted filtration[30] *via* a home-made stainless-steel mask with four fingers (length: 14 mm; width: 1 mm; interspace: 500 μm) on each side. Briefly, 3 mL of exfoliated graphene (EG) alcohol solution (0.1 $mg\ mL^{-1}$) was first deposited from the both sides of the mask on the flexible nylon membrane as highly-conductive metal-free current collector. Subsequently, 1 mL of NPCA active material solution (0.5 $mg\ mL^{-1}$ with 10 wt% EG) was continuously filtrated from the mask on the EG layer. After that, 2 mL of EG (0.02 mg mL^{-1}) was also deposited to form the electrically conductive network. After the mask was removed and the as-fabricated interdigital microelectrodes were carefully coated with polymer gel electrolyte of Na_2SO_4/polyvinyl alcohol (PVA), NPCA-MSCs were achieved. EG was prepared from anode exfoliation of graphite film in alkaline KOH aqueous solution, according to previous works [33,34].

2.4. Electrochemical measurements

In the aqueous electrolyte system, the working electrode was prepared by mixing the active material, polyvinylidene as the binder and carbon black as the conductive agent in a mass ratio of 8:1:1 followed by coating onto the Ni foam (1 cm^2) with a loading of 2 mg cm^{-2}. In the three-electrode system, the Pt foil, Hg/HgO electrode and 6 M KOH were used as the counter electrode, reference electrode and electrolyte, respectively. The aqueous-based symmetric supercapacitor devices were assembled using two working electrodes with a cellulose separator (NKK, MPF30AC-100) in 6 M KOH.

Cyclic voltammetry (CV), galvanostatic charge–discharge (GCD) profiles and electrochemical impedance spectroscopy (EIS) were tested using a CHI760E electrochemical workstation at room temperature. The EIS was recorded in a frequency range from 100 kHz to 0.01 Hz under open circuit potential with an amplitude of 5 mV.

3. Results and discussion

3.1. Preparation and characterization of NPCA

The synthesis procedure of NPCA is illustrated in Fig. 1. The gelatinous Zn-chitosan complex is formed *via* the chelation reaction by the coordination of Zn^{2+} and amino groups in chitosan. Subsequently, the as-obtained complex is freeze-dried to form Zn-chitosan aerogel, followed by carbonization at 800 °C for 2 h. The NPCA is prepared after washing with HCl and water thoroughly to remove the residual Zn^{2+}. For comparation, the NPC and dense CA are synthesized without freeze-drying and Zn^{2+} solution, respectively. TEM image in Fig. 2a shows the uniform and mesh-like features of NPCA with numerous pores. High-resolution TEM (HRTEM, Fig. 2b) image clearly displays that NPCA has small-sized mesopores in large scale and a small fraction of micropores, with thin walls only in several nanometers. The porous structure mainly originates from the removal of Zn^{2+} from the carbon skeleton [35,36]. SEM images (Fig. 2c and d) further reveal hierarchically porous configuration of NPCA, uniformly distributed on the continuous carbon network, with a 3D reticular texture. On a sharp contrast, NPC and CA represent rather dense surface without obvious pore structure (Fig. S1), manifesting the key function of Zn^{2+} coordination and freeze-drying procedures on the formation of final structure of NPCA. In principle, Zn^{2+} acts as the sacrificial template to produce pores and the cross-linking structure of Zn-chitosan complex can be finely maintained without collapsing under freeze-drying condition instead of directly drying. It is worth noting that the interconnected pores and continuous carbon framework are beneficial for rapid ion diffusion and fast electron transport. Additionally, such 3D reticular architecture can offer ultrahigh SSA for large specific capacitance. The EDX mapping images (Fig. 2e) indicate that N and O elements are uniformly distributed in the carbon framework of NPCA.

SSA and pore structure are two essential parameters to evaluate carbon materials. The N_2 adsorption-desorption isotherms of NPCA, NPC and CA (Fig. 3a) display significant hysteresis loops and belong to the typical type-IV isotherm, indicating the presence of abundant mesopores [37]. The sharp slopes appear at low relative pressure (close to 0) imply that micropores exist in the samples [38]. This is consistent with the TEM and SEM results. According to the pore size distributions calculated by nonlocal density functional theory (NLDFT) (inset in Fig. 3a), NPCA shows two peaks locating at ~1.5 nm (micropore) and ~3 nm (mesopore). It is well known that micropores can create more absorption sites and small-sized mesopores in the range of 3–5 nm are required to improve the capacitance in electric double layer capacitors (EDLCs) [26,27]. NPC exhibits similar pore size distribution with NPCA except portion of large mesopores centering ~20 nm. While CA possesses smaller micropores (~1.2 nm) and a wide distribution of mesopores. Both NPC and CA contain lower peaks intensity at pore area compared to NPCA. Undoubtedly, NPCA has much larger SSA (2529 m^2 g^{-1}) and total pore volume (1.49 cm^3g^{-1}) than those of NPC (1622 m^2 g^{-1}, 1.36 cm^3g^{-1}) and CA (655 m^2 g^{-1}, 0.51 cm^3g^{-1}) (Table S1). Moreover, both NPCA and NPC possess mesopore volume ratio higher than 85.9% (Table S1), further conforming the development of mesopores are mostly boosted by Zn^{2+}.

Fig. 3b shows the XRD patterns of NPCA, NPC and CA. Two broad peaks at around 23° and 43° can be identified of all samples, confirming the amorphous structure of these carbon materials [39,40]. The sharp peak at 26.5° is assigned to (002) plane of graphitic carbon, demonstrating a certain degree of graphitization of CA [41]. The amorphous nature is further verified by Raman spectra (Fig. 3c), which display two characteristic peaks at ~1333 cm^{-1} (D band) and ~1600 cm^{-1} (G band) associated with the structural defects and vibration of carbon atoms [42,43]. The I_D/I_G values of NPCA, NPC and CA decrease from 1.14 to 1.08 and 1.01, suggesting the highly amorphous feature of NPCA, which is attributed to the 3D porous

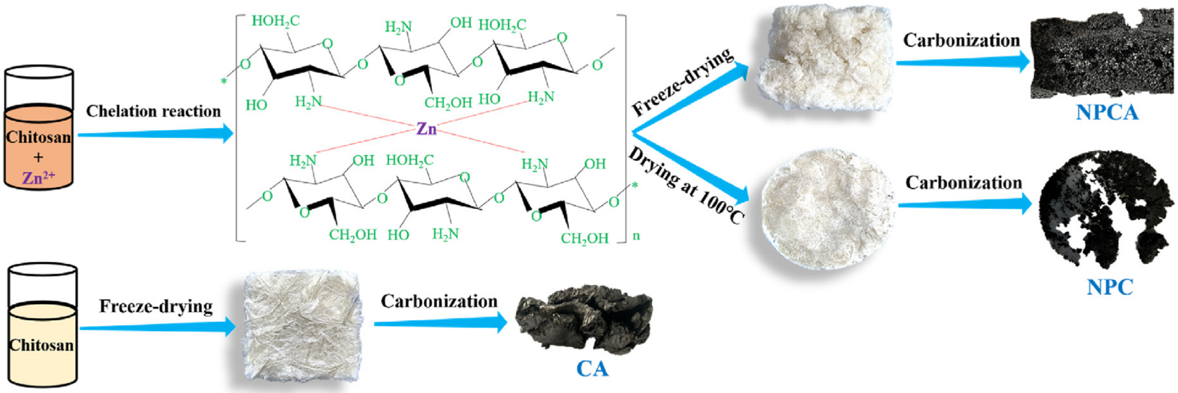

Fig. 1. The schematic synthesis routes of NPCA, NPC and CA. (A colour version of this figure can be viewed online.)

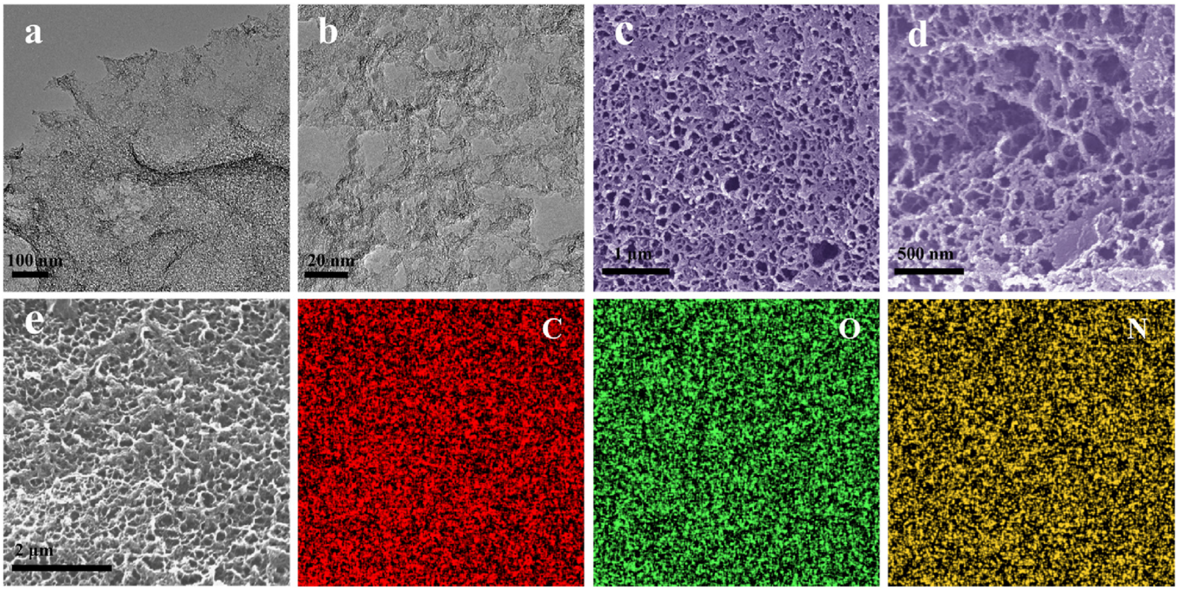

Fig. 2. (a) TEM, (b) HRTEM, (c, d, e) SEM images and the corresponding EDX mapping of C, O, N elements of NPCA. (A colour version of this figure can be viewed online.)

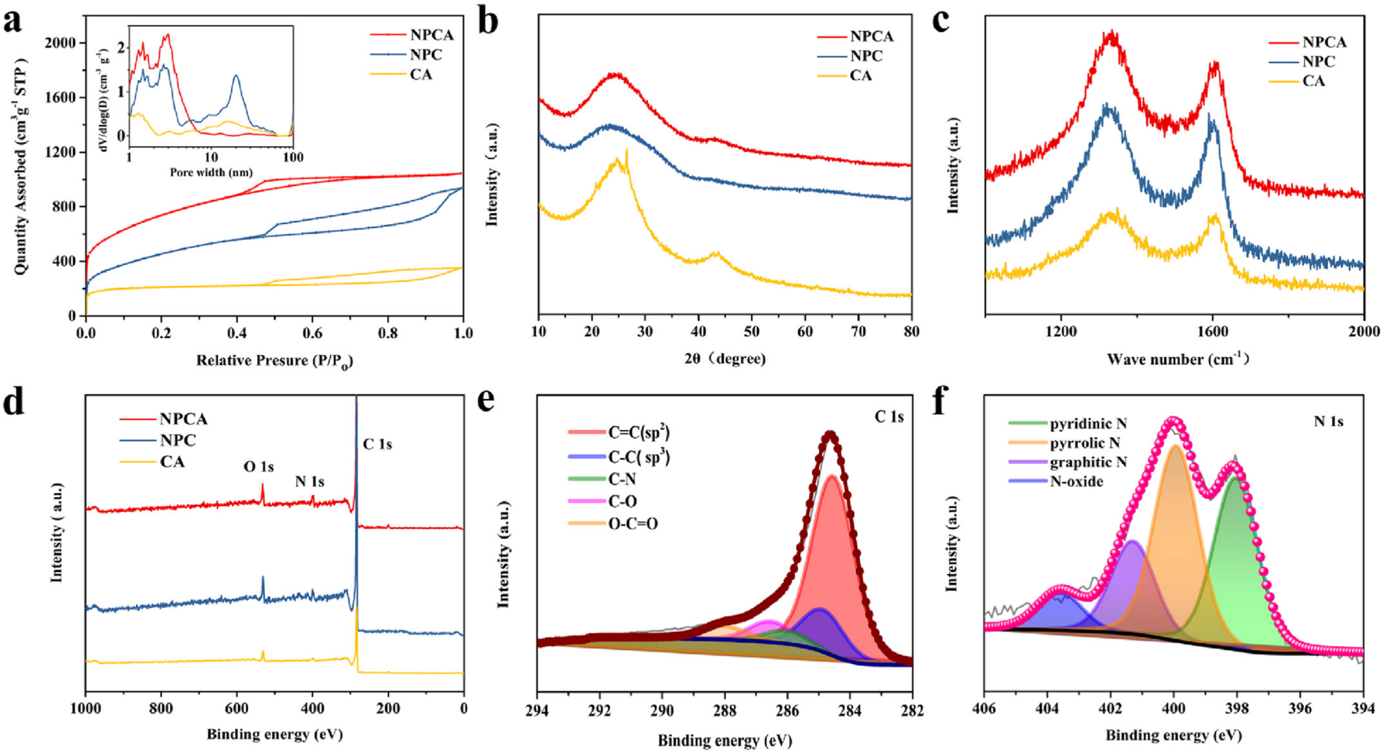

Fig. 3. (a) Nitrogen absorption-desorption isotherms (inset: pore size distribution), (b) XRD patterns, (c) Raman spectra and (d) XPS survey spectra of NPCA, NPC and CA. (e) C 1s and (f) N 1s high-resolution XPS spectra of NPCA. (A colour version of this figure can be viewed online.)

structure and nitrogen doping. The XPS surveys (Fig. 3d) confirm the existence of C, N, and O atoms in the three materials. As shown in Fig. 3e, high-resolution XPS spectrum of C 1s in NPCA is configured to five peaks, corresponding to C═C (284.6 eV), C—C (285.0 eV), C—N (286.0 eV), C—O (286.5 eV) and C═O (288.0 eV), respectively [44,45]. For N 1s spectrum (Fig. 3f), four peaks can be deconvoluted locating at 398.1 eV (pyridinic-N, 2.56 wt%), 399.9 eV (pyrrolic—N, 2.91 wt%), 401.3 eV (quaternary-N, 1.39 wt%) and 403.6 eV (oxidized-N, 0.56 wt%), respectively [46]. NPCA possesses the highest N content of 7.42 wt% (Table S2). Notably, it is reported that the pyridinic-/pyrrolic-N functionalities with unpaired electrons are more active than other nitrogen species for the improvement of capacitance [47]. The quaternary-N functionality locating at the middle of graphite are considered to boost electron transport through the carbon plane by disturbance of electron density in the π-system [48]. With a high proportion of the above three N species to the total N content, NPCA is expected to display better energy storage ability.

3.2. Electrochemical performance in three-electrode system

The electrochemical performance of NPCA compared with NPC and CA is first evaluated in a three-electrode system using 6 M KOH aqueous electrolyte. Cyclic voltammetry (CV) curves (Fig. 4a) of NPCA, NPC and CA exhibit almost symmetric rectangular shape at scan rate of 20 mV s^{-1}, suggesting the obviously quasi-EDLC behavior [49]. Higher capacitance of NPCA than those of NPC and CA can be confirmed from the larger current density of CV result, as a result of 3D reticular architecture with interconnected micro-/mesoporous structure, high N doping and super large SSA for NPCA. As the scan rate increases from 5 to 100 mV s^{-1}, the shapes of the CV curves are well sustained (Fig. 4b), demonstrating the excellent kinetic reversibility and high rate capability of NPCA. The superior electrochemical performance of NPCA is also unraveled by galvanostatic charge-discharge (GCDs) tests. The GCD profiles with triangular shape also reveal the typical EDLC feature of these three samples (Fig. 4c). NPCA displays much longer discharge time compared with NPC and CA, further reflecting the advantage of 3D reticular structure for capacitance enhancement. In addition, the GCD profiles of NPCA, NPC and CA are measured at various current densities ranging from 0.5 to 10 A g^{-1} (Figs. 4d and S2). As expected, NPCA declares higher capacitance than NPC and CA electrodes at all current densities (Fig. 4e), underlying the importance of Zn^{2+} co-ordination and freeze-drying for electrochemical performance improvement. Significantly, NPCA can reach up to a high capacitance of 267 F g^{-1} at 1 A g^{-1} and still maintain 86.3% (230 F g^{-1}) of initial capacitance at the large current density of 10 A g^{-1}, implying outstanding rate capability. According to the EIS (Fig. 4f), NPCA exhibits lower serial resistance (R_s: 0.36 Ω) and charge transfer resistance (R_{ct}: 0.07 Ω) than those of NPC (R_s: 0.42 Ω; R_{ct}: 0.09 Ω) and CA (R_s: 0.61 Ω; R_{ct}: 0.17 Ω), illustrating the exceptional electrochemical properties of NPCA. Moreover, the nearly vertical line at low frequency region of NPCA manifests the extremely low ionic diffusion resistance. The cycling performance of NPCA is estimated by continuous GCD test at 5 A g^{-1} (Fig. 5a), showing no capacitance fading and a coulombic efficiency of 100% after 10000 cycles. Thus, the Nyquist plots before and after the cycling test are almost coincident (Fig. 5b), further underscoring the excellent long-term durability of NPCA.

3.3. Aqueous-based NPCA-SC

In order to demonstrate the practical application of NPCA, the symmetric SC is further constructed using 6 M KOH electrolyte (NPCA-SC). The CV measurements are conducted at different scan rates of 5–100 mV s^{-1}, and GCD tests are carried out at various current densities of 0.5–10 A g^{-1}. The rectangular CV curves (Fig. 6a) and triangular GCD profiles (Fig. 6b) prove the EDLC nature of NPCA-SC. Notably, even at high scan rate of 100 mV s^{-1}, the CV shape is still retained the same, indicating the fast and reversible reactions. Outstanding specific capacitance of NPCA-SC calculated from GCD results is shown in Fig. S3a. It presents a high specific capacitance of 195 F g^{-1} at 0.5 A g^{-1} and maintains 132 F g^{-1} at 10 A g^{-1} with a capacitance retention of 67.7%, illustrating exceptional rate performance. Nyquist plot of NPCA-SC with small semicircle, low R_s value together with the straight line nearly perpendicular to the real axis underscore its good electrical conductivity and rapid charge transport (Fig. S3b). Importantly, NPCA-SC shows excellent charge-discharge cycling stability, only 9% capacitance attenuating after 10000 cycles at 1 A g^{-1} (Fig. 6c). Ragone plots are used to compare our NPCA-SC with other

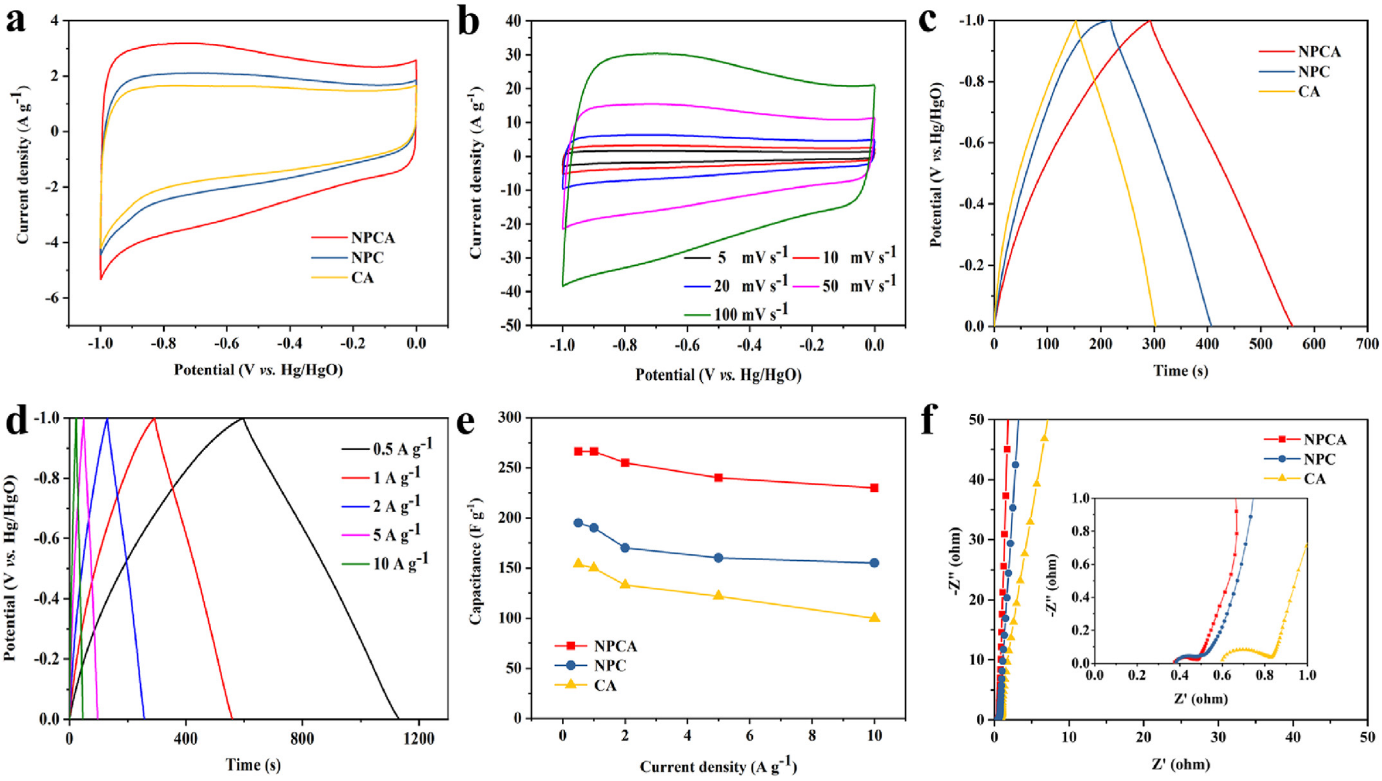

Fig. 4. Electrochemical performance of NPCA, NPC and CA in three-electrode system using 6 M KOH electrolyte. (a) CV curves of NPCA, NPC and CA at 20 mV s^{-1}. (b) CV curves of NPCA at different scan rates. (c) GCD profiles of NPCA, NPC and CA at 1 A g^{-1}. (d) GCD profiles of NPCA at different current densities. (e) Specific capacitances of NPCA, NPC and CA at various current densities. (f) Nyquist plots of NPCA, NPC and CA. Inset: magnified curves at high frequency region. (A colour version of this figure can be viewed online.)

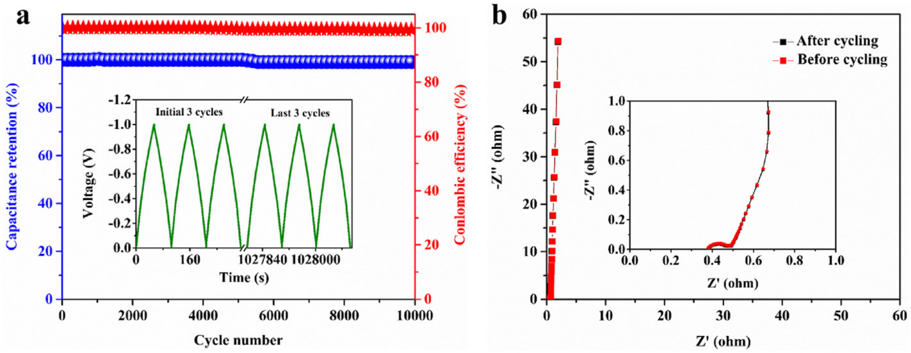

Fig. 5. (a) Cycling performance of NPCA at 5 A g^{-1}. Inset is the GCD profiles before and after cycling. (b) Nyquist plots of NPCA before and after cycling test. Inset: magnified curves at high frequency region. (A colour version of this figure can be viewed online.)

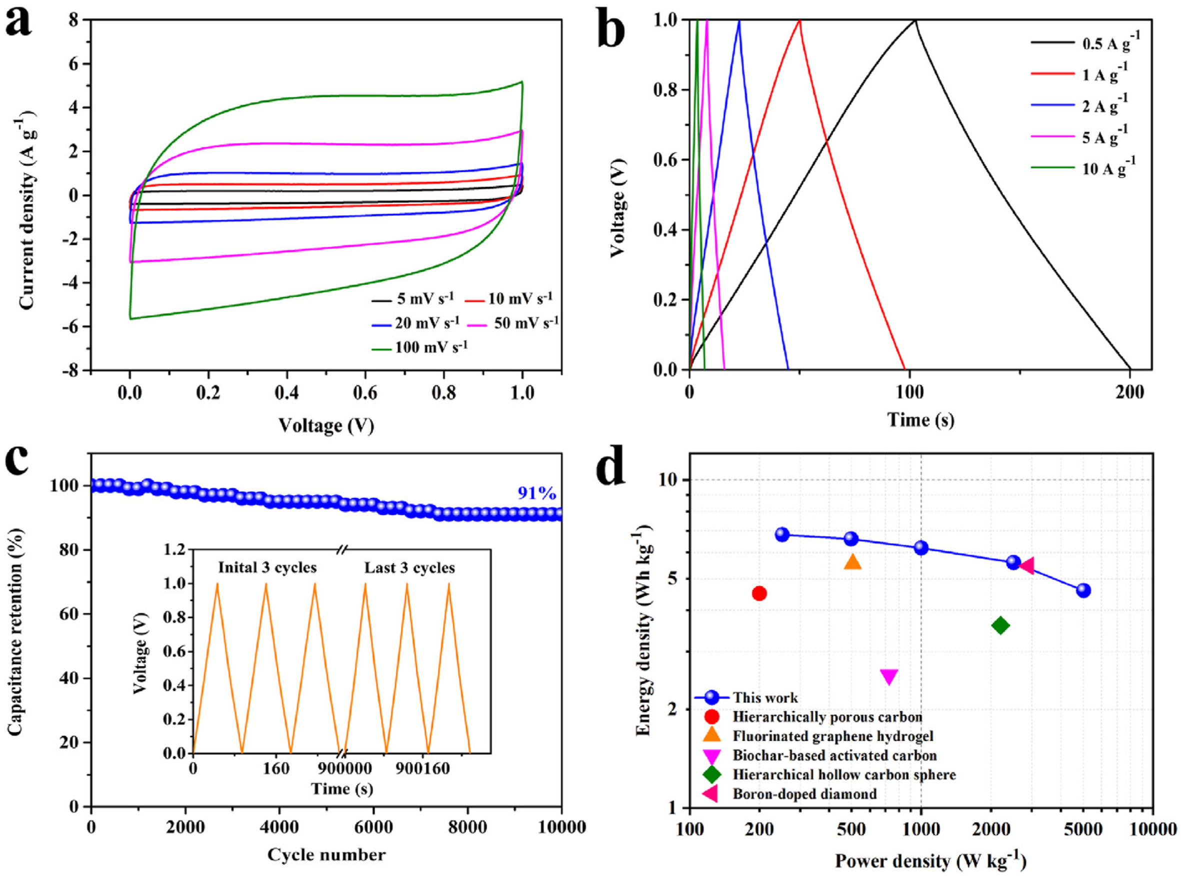

Fig. 6. Electrochemical performance of NPCA-SC: (a) CV curves at different scan rates, (b) GCD profiles at various current densities, (c) long-term cycling stability at 1 A g^{-1} for 10000 cycles and (d) Ragone plots compared with carbon-based symmetric supercapacitors. (A colour version of this figure can be viewed online.)

heteroatom-doped carbon-based symmetric SCs previously reported (Fig. 6d). Impressively, NPCA-SC discloses high energy density of 6.8 Wh kg^{-1} at power density of 251 W kg^{-1}, outperforming the symmetric SCs of hierarchically porous carbon (4.5 Wh kg^{-1}) [50], fluorinated graphene hydrogel (5.6 Wh kg^{-1}) [51], biochar-based activated carbon (2.54 Wh kg^{-1}) [52], hierarchical hollow carbon sphere (3.6 Wh kg^{-1}) [53] and boron-doped diamond (5.5 Wh kg^{-1}) [54]. Further, NPCA-SC can still reach an energy density of 4.6 Wh kg^{-1} when the power density goes up to 5.0 kW kg^{-1}, implying the extraordinary potential for the real application.

3.4. Solid-state NPCA-MSC

To meet the high requirement of the miniaturized and wearable electronics, we fabricate flexible symmetric MSCs based on the as-prepared NPCA with a mass loading of 0.25 mg cm^{-2} (denoted as NPCA-MSC, ~10 μm in thickness) on a smooth filter membrane substrate through a mask-assisted filtration strategy, where EG is used as flexible current collector and conductive additives [55]. As shown in Fig. 7a, when the fabricated NPCA-MSC is bended and twisted into the deformable shapes, the structural intensity of the interdigital micro-electrodes can be retained without delamination from the substrate, showing excellent flexibility. The

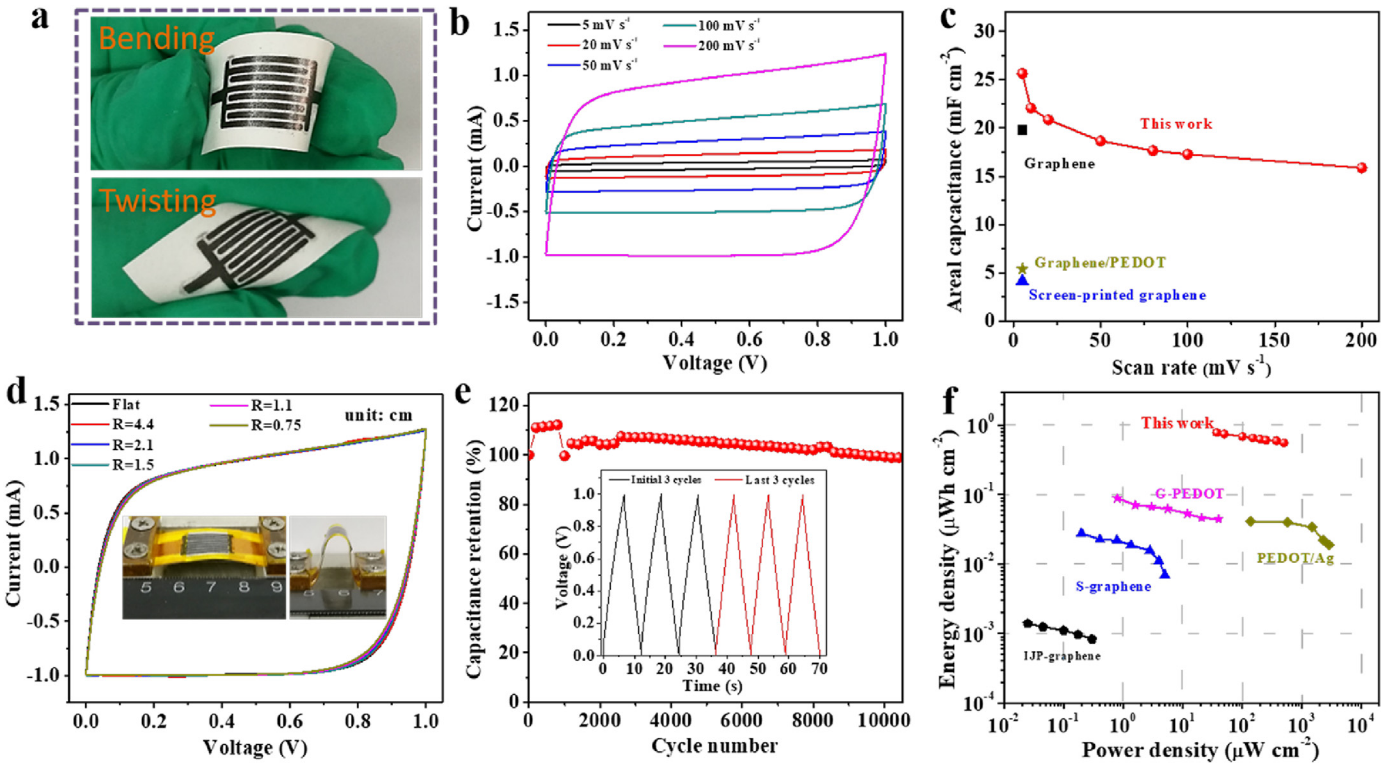

Fig. 7. Electrochemical performance of solid-state NPCA-MSC: (a) digital photos at different bending states, (b) CV curves at different scan rates, (c) areal capacitance obtained from 5 to 200 mV s^{-1}, (d) CV curves at different R (Inset: photographs of devices at R = 0.75 cm and flat), (e) cycling stability obtained at 1.5 mA cm^{-2} (Inset: GCD profiles before and after cycling) and (f) Ragone plots compared with the reported carbon-based MSCs. (A colour version of this figure can be viewed online.)

electrochemical performance of NPCA-MSC is evaluated in the voltage of 1.0 V by CV curves, GCD profiles and EIS measurements in Na_2SO_4/PVA gel electrolyte. The CV curves (Fig. 7b) tested from 5 to 200 mV s^{-1} present obviously rectangular shapes, and the GCD profiles measured from 75 to 1000 μA cm^{-2} demonstrate nearly symmetrical triangle features (Fig. S4a), suggesting the ideal EDLC behavior. The areal capacitances of NPCA-MSC calculated from CV and GCD measurements are recorded in Fig. 7c and Fig. S4b, respectively. Our device offers high areal capacitance of 25.6 mF cm^{-2} at scan rate of 5 mV s^{-1}, which is superior to many reported carbon-based MSCs, such as graphene (19.5 mF cm^{-2}) [56], screen-printed graphene (4.16 mF cm^{-2}) [57], graphene/PEDOT (5.4 mF cm^{-2}) [58]. Furthermore, when the scan rate reaches up to 200 mV s^{-1}, the NPCA-MSC still retains areal capacitance of 15.9 mF cm^{-2}, which is 62% of the initial capacitance, indicating the robust rate performance. The notable rate capability of the NPCA-MSC is attributed to high electrical conductivity together with rapid ion diffusion of NPCA and EG. This can be elucidated by the EIS results (Fig. S5), which reveals a small equivalent R_s of 36 Ω and high slope of diagonal line. To eliminate the capacitance contribution of EG, an EG-MSC constructed by pure EG with the same mass loading (0.25 mg cm^{-2}) of NPCA-MSC is fabricated. The EG-MSC shows negligible integrated area in CV curves and charge-discharge time in GCD profiles compared with NPCA-MSC (Fig. S6). The effect of microelectrode thickness on the areal capacitance is also investigated by comparing the electrochemical performance of NPCA-MSC with NPCA-MSC-0.5 (mass loading: 0.5 mg cm^{-2}; thickness: ~20 μm) and NPCA-MSC-1.0 (mass loading: 1.0 mg cm^{-2}; thickness: ~40 μm) (Figs. S7 and S8). With electrode thickness increasing, the MSC delivers higher areal capacitance but much lower rate capability, which is mainly attributed to the limited ion diffusion in thick microelectrodes, as demonstrated by EIS spectra (Fig. S8d).

We further test the flexibility and bending durability of NPCA-MSC. Remarkably, it is observed that all the CV curves of NPCA-MSC are almost overlapped as the bending radius of curvature (R) decreasing from flat to 0.75 cm (corresponding bending angles of 0° and 180°) with a capacitance retention of 99% (Figs. 7d and S9), verifying outstanding structural stability and mechanical flexibility of our MSC. Especially, NPCA-MSC displays unchanged capacitance after repeating bending at R = 0.75 cm for 1000 times (Fig. S10), suggestive of the promising application for flexible devices. More importantly, NPCA-MSC exhibits excellent cycling stability with a capacitance retention of more than 99% after 10000 cycles at 1.5 mA cm^{-2} (Fig. 7e). Ragone plots in Fig. 7f show the areal energy density and power density of our MSC compared with the previously reported carbon-based MSCs. NPCA-MSC possesses a high areal energy density of 0.78 μWh cm^{-2} at power density of 37.48 μW cm^{-2}, and even preserves an areal energy density of 0.56 μWh cm^{-2} at high power density of 500 μW cm^{-2}, well comparable to the previous MSCs such as ink-jet printing graphene (IJP-graphene, 0.0014 μWh cm^{-2} at 0.025 μW cm^{-2}) [59], poly(3,4-ethylenedioxythiophene) (PEDOT)/Ag (0.041 μWh cm^{-2} at 138 μW cm^{-2}) [60], spray-coated graphene (S-graphene, 0.028 μWh cm^{-2} at 0.2 μW cm^{-2}) and graphene/PEDOT (G-PEDOT, 0.089 μWh cm^{-2} at 0.8 μW cm^{-2}) [61].

The excellent electrochemical performance of NPCA-SC and solid-state NPCA-MSC is ascribed to the unique hierarchically pore structure and synergistic utilization of each advantage over NPCA, incentivized by Zn^{2+} coordination and freeze-drying methods. First, 3D reticular texture makes it to generate extremely high SSA (2529 m^2 g^{-1}), which is responsible for abundant ion adsorption, and thus enhancing the energy storage. Second, the interlinked and uniform micro-/mesopores distribution enhance the capacitive performance, in which the micropores create more sites for ion adsorption and the mesopores offer interconnected ion channels for fast ion diffusion. Third, continuous carbon skeleton provides high electrical conductivity for rapid electron transport and allows it to form electric double layers. Last but not least, nitrogen incorporation produces numerous electrochemically active sites for offering additional capacitance (*e.g.*, pyridinic-/pyrrolic-N functionalities) and advancing the electrical conductivity (*e.g.*, quaternary-N functionality).

4. Conclusions

In summary, we have developed a universal cost-effective method utilizing chelation reaction and freeze-drying to synthesize robust NPCA with 3D reticular texture for high-quality aqueous-based symmetric SCs and solid-state flexible MSC. The as-assembled NPCA-SC presents remarkable electrochemical performance with high specific capacitance of 195 F g^{-1} at 0.5 A g^{-1}, excellent cycling stability with 91% capacitance retention after 10000 cycles at 1 A g^{-1} and enhanced energy density of 6.8 Wh kg^{-1} at power density of 251 W kg^{-1}. The as-fabricated solid-state NPCA-MSC delivers high areal capacitance of 25.6 mF cm^{-2}, outstanding energy density of 0.78 μWh cm^{-2}, exceptional cyclability with only 1% capacitance fading after 10000 cycles, as well as superior flexibility. Therefore, our strategy opens a new avenue for the fabrication of biomass derived carbon aerogels as high-capacitance electrode materials applied in SCs and flexible MSCs.

CRediT authorship contribution statement

Yunfang Gao: Conceptualization, Investigation, Resources. **Shuanghao Zheng:** Data curation, Writing - original draft. **Hanli Fu:** Methodology, Data curation, Writing - original draft. **Jiaxin Ma:** Data curation. **Xin Xu:** Investigation. **Li Guan:** Data curation. **Haihua Wu:** Conceptualization, Supervision, Writing - original draft, Writing - review & editing. **Zhong-Shuai Wu:** Supervision, Writing - original draft, Writing - review & editing.

Declaration of competing interest

The authors declare that they have no known competing financial interests or personal relationships that could have appeared to influence the work reported in this paper.

Acknowledgement

This work was financially supported by the National Natural Science Foundation of China (Grants 51872283 and 21805273), National Key Research and Development Project of China (Grant 2016YFC0305004), Zhejiang Provincial Key Research and Development Project (Grants 2018C03032 and 2019C01094), General Scientific Research Project of Zhejiang Provincial Education Department (Grant Y201941064), Liaoning Revitalization Talents Program (Grant XLYC1807153), Natural Science Foundation of Liaoning Province, Joint Research Fund Liaoning-Shenyang National Laboratory for Materials Science (Grant 20180510038), DICP (Grants ZZBS201708 , ZZBS201802 and DICP I202032), DICP&QIBEBT (Grant DICP&QIBEBT UN201702), Dalian National Laboratory For Clean Energy, DNL Cooperation Fund, CAS (Grants DNL180310, DNL180308, DNL201912, and DNL201915).

Appendix A. Supplementary data

Supplementary data to this article can be found online at https://doi.org/10.1016/j.carbon.2020.06.063.

References

[1] X. Rui, H. Tan, Q. Yan, Nanostructured metal sulfides for energy storage, Nanoscale 6 (2014) 9889–9924.

[2] L. Manjakkal, W.T. Navaraj, C.G. Nunez, R. Dahiya, Graphene-graphite polyurethane composite based high-energy density flexible supercapacitors, Adv. Sci. 6 (2019) 1802251.

[3] D. Yu, Q. Qian, L. Wei, W. Jiang, K. Goh, J. Wei, J. Zhang, Y. Chen, Emergence of fiber supercapacitors, Chem. Soc. Rev. 44 (2015) 647–662.

[4] L.L. Zhang, X.S. Zhao, Carbon-based materials as supercapacitor electrodes, Chem. Soc. Rev. 38 (2009) 2520–2531.

[5] P. Simon, Y. Gogotsi, B. Dunn, Where do batteries end and supercapacitors begin? Science 343 (2014) 1210–1211.

[6] T.G. Yun, D. Kim, Y.H. Kim, M. Park, S. Hyun, S.M. Han, Photoresponsive smart coloration electrochromic supercapacitor, Adv. Mater. 29 (2017) 1606728.

[7] Z.-S. Wu, A. Winter, L. Chen, Y. Sun, A. Turchanin, X. Feng, K. Müllen, Three-dimensional nitrogen and boron co-doped graphene for high-performance all-solid-state supercapacitors, Adv. Mater. 24 (2012) 5130–5135.

[8] S.-H. Kim, K.-H. Choi, S.-J. Cho, J. Yoo, S.-S. Lee, S.-Y. Lee, Flexible/shape-versatile, bipolar all-solid-state lithium-ion batteries prepared by multistage printing, Energy Environ. Sci. 11 (2018) 321–330.

[9] M. Yousaf, H.T.H. Shi, Y. Wang, Y. Chen, Z. Ma, A. Cao, H.E. Naguib, R.P.S. Han, Flexible electronics: novel pliable electrodes for flexible electrochemical energy storage devices: recent progress and challenges, Adv. Energy Mater. 6 (2016) 1600490.

[10] X. Lu, C. Wang, F. Favier, N. Pinna, Electrospun nanomaterials for supercapacitor electrodes: designed architectures and electrochemical performance, Adv. Energy Mater. 7 (2016) 1601301.

[11] W. Zhang, Q. Jiang, Y. Lei, H.N. Alshareef, Wettability-driven assembly of electrochemical microsupercapacitors, ACS Appl. Mater. Interfaces 11 (2019) 20905–20914.

[12] S.T. Senthilkumar, R.K. Selvan, J.S. Melo, Redox additive/active electrolytes: a novel approach to enhance the performance of supercapacitors, J. Mater. Chem. 1 (2013) 12386–12394.

[13] D. Hulicova-Jurcakova, M. Seredych, G.Q. Lu, T.J. Bandosz, Combined effect of nitrogen- and oxygen-containing functional groups of microporous activated carbon on its electrochemical performance in supercapacitors, Adv. Funct. Mater. 19 (2009) 438–447.

[14] J. Zhang, G. Chen, Q. Zhang, F. Kang, B. You, Self-assembly synthesis of N-doped carbon aerogels for supercapacitor and electrocatalytic oxygen reduction, ACS Appl. Mater. Interfaces 7 (2015) 12760–12766.

[15] D. Pech, M. Brunet, H. Durou, P. Huang, V. Mochalin, Y. Gogotsi, P.L. Taberna, P. Simon, Ultrahigh-power micrometre-sized supercapacitors based on onion-like carbon, Nat. Nanotechnol. 5 (2010) 651–654.

[16] S. Boukhalfa, K. Evanoff, G. Yushin, Atomic layer deposition of vanadium oxide on carbon nanotubes for high-power supercapacitor electrodes, Energy Environ. Sci. 5 (2012) 6872–6879.

[17] C. Liu, Z. Yu, D. Neff, A. Zhamu, B.Z. Jang, Graphene-based supercapacitor with an ultrahigh energy density, Nano Lett. 10 (2010) 4863–4868.

[18] L. Chen, H. Dai, Y. Zhou, Y. Hu, T. Yu, J. Liu, Z. Zou, Porous, single crystalline titanium nitride nanoplates grown on carbon fibers: excellent counter electrodes for low-cost, high performance, fiber-shaped dye-sensitized solar cells, Chem. Commun. 50 (2014) 14321–14324.

[19] J. Biener, M. Stadermann, M. Suss, M.A. Worsley, M.M. Biener, K.A. Rose, T.F. Baumann, Advanced carbon aerogels for energy applications, Energy Environ. Sci. 4 (2011) 656–667.

[20] G.L. Sun, H.Y. Xie, J.B. Ran, L.Y. Ma, X.Y. Shen, J.M. Hu, H. Tong, Rational design of uniformly embedded metal oxide nanoparticles into nitrogen-doped carbon aerogel for high-performance asymmetric supercapacitors with a high operating voltage window, J. Mater. Chem. 4 (2016) 16576–16587.

[21] J.R. Miller, P. Simon, Electrochemical capacitors for energy management, Science 321 (2008) 651–652.

[22] C. Ping, T. Li, Y. Hang, Z. Lei, Z. Liu, Z. Lei, Biomass-derived carbon fiber aerogel as a binder-freeelectrode for high-rate supercapacitors, J. Phys. Chem. C 120 (2016) 2079–2086.

[23] P. Hao, Z. Zhao, J. Tian, H. Li, Y. Sang, G. Yu, H. Cai, H. Liu, C.P. Wong, A. Umar, Hierarchical porous carbon aerogel derived from bagasse for high performance supercapacitor electrode, Nanoscale 6 (2014) 12120–12129.

[24] H. Liu, Y. Zhang, Q. Ke, K.H. Ho, Y. Hu, J. Wang, Tuning the porous texture and specific surface area of nanoporous carbons for supercapacitor electrodes by adjusting the hydrothermal synthesis temperature, J. Mater. Chem. 1 (2013) 12962.

[25] X. Deng, J. Li, S. Zhu, L. Ma, N. Zhao, Boosting the capacitive storage performance of MOF-derived carbon frameworks via structural modulation for supercapacitors, Energy Storage Mater. 23 (2019) 491–498.

[26] K.H. An, W.S. Kim, Y.S. Park, H.J. Jeong, Y.C. Choi, J.M. Moon, D.J. Bae, S.C. Lim, Y.H. Lee, Supercapacitors using singlewalled carbon nanotube electrodes, Adv. Mater. 13 (2001) 497–500.

[27] H. Zhou, S. Zhu, M. Hibino, I. Honma, Electrochemical capacitance of self-ordered mesoporous carbon, J. Power Sources 122 (2003) 219.

[28] L.F. Chen, X.D. Zhang, H.W. Liang, M.G. Kong, Q.F. Guan, P. Chen, Z.Y. Wu, S.H. Yu, Synthesis of nitrogen-doped porous carbon nanofibers as an efficient electrode material for supercapacitors, ACS Nano 6 (2012) 7092–7102.

[29] C.J. Wang, D.P. Wu, H.J. Wang, Z.Y. Gao, F. Xu, K. Jiang, A green and scalable

route to yield porous carbon sheets from biomass for supercapacitors with high capacity, J. Mater. Chem. 6 (2018) 1244–1254.
[30] D.D. Shan, J. Yang, W. Liu, J. Yan, Z.J. Fan, Biomass-derived three-dimensional honeycomb-like hierarchical structured carbon for ultrahigh energy density asymmetric supercapacitors, J. Mater. Chem. 4 (2016) 13589–13602.
[31] S. Selvam, B. Balamuralitharan, S. Jegatheeswaran, M.-Y. Kim, S.N. Karthick, J. Anandha Raj, P. Boomi, M. Sundrarajan, K. Prabakar, H.-J. Kim, Electrolyte-imprinted graphene oxide-chitosan chelate with copper crosslinked composite electrodes for intense cyclic-stable, flexible supercapacitors, J. Mater. Chem. 5 (2017) 1380–1386.
[32] M.N.V. Ravi Kumar, A review of chitin and chitosan applications, React. Funct. Polym. 46 (2000) 1–27.
[33] Z.-S. Wu, K. Parvez, X. Feng, K. Müllen, Photolithographic fabrication of high-performance all-solid-state graphene-based planar micro-supercapacitors with different interdigital fingers, J. Mater. Chem. 2 (2014) 8288–8293.
[34] F. Zhou, H. Huang, C. Xiao, S. Zheng, X. Shi, J. Qin, Q. Fu, X. Bao, X. Feng, K. Müllen, Z.-S. Wu, Electrochemically Scalable production of fluorine-modified graphene for flexible and high-energy ionogel-based micro-supercapacitors, J. Am. Chem. Soc. 140 (2018) 8198–8205.
[35] L. Jiang, L. Sheng, X. Chen, T. Wei, Z. Fan, Construction of nitrogen-doped porous carbon buildings using interconnected ultra-small carbon nanosheets for ultra-high rate supercapacitors, J. Mater. Chem. 4 (2016) 11388–11396.
[36] B. Li, Y. Cheng, L. Dong, Y. Wang, J. Chen, C. Huang, D. Wei, Y. Feng, D. Jia, Y. Zhou, Nitrogen doped and hierarchically porous carbons derived from chitosan hydrogel via rapid microwave carbonization for high-performance supercapacitors, Carbon 122 (2017) 592–603.
[37] J. Jin, X. Qiao, F. Zhou, Z.-S. Wu, L. Cui, H. Fan, Interconnected phosphorus and nitrogen codoped porous exfoliated carbon nanosheets for high-rate supercapacitors, ACS Appl. Mater. Interfaces 9 (2017) 17317–17325.
[38] C. Li, W. Wu, P. Wang, W. Zhou, J. Wang, Y. Chen, L. Fu, Y. Zhu, Y. Wu, W. Huang, Fabricating an aqueous symmetric supercapacitor with a stable high working voltage of 2 V by using an alkaline–acidic electrolyte, Adv. Sci. 6 (2019) 1801665.
[39] L.F. Chen, Y. Lu, L. Yu, X.W. Lou, Designed formation of hollow particle-based nitrogen-doped carbon nanofibers for high-performance supercapacitors, Energy Environ. Sci. 10 (2017) 1777–1783.
[40] Z. Li, C. Wang, X. Chen, X. Wang, X. Li, Y. Yamauchi, X. Xu, J. Wang, C. Lin, D. Luo, X. Wang, X.S. Zhao, MoO_x nanoparticles anchored on N-doped porous carbon as Li-ion battery electrode, Chem. Eng. J. 381 (2020) 122588.
[41] H. Zhu, L. Gu, D.N. Yu, Y.J. Sun, M. Wan, M. Zhang, L. Wang, L.N. Wang, W.W. Wu, J.M. Yao, M.L. Du, S.J. Guo, The marriage and integration of nanostructures with different dimensions for synergistic electrocatalysis, Energy Environ. Sci. 10 (2017) 321–330.
[42] L.F. Chen, Z.H. Huang, H.W. Liang, H.L. Gao, S.H. Yu, Three-dimensional heteroatom-doped carbon nanofiber networks derived from bacterial cellulose for supercapacitors, Adv. Funct. Mater. 24 (2014) 5104–5111.
[43] A. Reina, X. Jia, J. Ho, D. Nezich, J. Kong, Layer Area, Few-layer graphene films on arbitrary substrates by chemical vapor deposition, Nano Lett. 9 (2009) 30–35.
[44] L. Hu, Y. Liao, D. Xia, F. Peng, L. Tan, S. Hu, C. Zheng, X. Lu, C. He, D. Shu, Engineered photocatalytic fuel cell with oxygen vacancies-rich $rGO/BiO_{1-X}I$ as photoanode and biomass-derived N-doped carbon as cathode: promotion of reactive oxygen species production via Fe^{2+}/Fe^{3+} redox, Chem. Eng. J. 385 (2020) 123824.
[45] X. Tong, Z. Chen, H. Zhuo, Y. Hu, S. Jing, J. Liu, L. Zhong, Tailoring the physicochemical properties of chitosan-derived N-doped carbon by controlling hydrothermal carbonization time for high-performance supercapacitor application, Carbohydr. Polym. 207 (2019) 764–774.
[46] D. Zhu, J. Jiang, D. Sun, X. Qian, Y. Wang, L. Li, Z. Wang, X. Chai, L. Gan, M. Liu, A general strategy to synthesize high-level N-doped porous carbons via Schiff-base chemistry for supercapacitors, J. Mater. Chem. 6 (2018) 12334–12343.
[47] Z. Li, Z. Xu, X. Tan, H. Wang, C.M.B. Holt, T. Stephenson, B.C. Olsen, D. Mitlin, Mesoporous nitrogen-rich carbons derived from protein for ultra-high capacity battery anodes and supercapacitors, Energy Environ. Sci. 6 (2013) 871–878.
[48] M. Seredych, D. Hulicova-Jurcakova, G.Q. Lu, T.J. Bandosz, Surface functional groups of carbons and the effects of their chemical character, density and accessibility to ions on electrochemical performance, Carbon 46 (2008) 1475–1488.
[49] Y. Zhang, X. Xu, Y. Gao, D. Gao, Z. Wei, H. Wu, *In-situ* synthesis of three-dimensionally flower-like $Ni_3V_2O_8$@carbon nanotubes composite through self-assembling for high performance asymmetric supercapacitors, J. Power Sources 455 (2020) 227985.
[50] F. Miao, C. Shao, X. Li, K. Wang, N. Lu, Y. Liu, Three-dimensional freestanding hierarchically porous carbon materials as binder-free electrodes for supercapacitors: high capacitive property and long-term cycling stability, J. Mater. Chem. 4 (2016) 5623–5631.
[51] H. An, Y. Li, P. Long, Y. Gao, C. Qin, C. Cao, Y. Feng, W. Feng, Hydrothermal preparation of fluorinated graphene hydrogel for high-performance supercapacitors, J. Power Sources 312 (2016) 146–155.
[52] N. He, S. Yoo, J. Meng, O. Yildiz, P.D. Bradford, S. Park, W. Gao, Engineering biorefinery residues from loblolly pine for supercapacitor applications, Carbon 120 (2017) 304–312.
[53] X. Yang, Y. Li, P. Zhang, L. Sun, X. Ren, H. Mi, Hierarchical hollow carbon spheres: novel synthesis strategy, pore structure engineering and application for micro-supercapacitor, Carbon 157 (2020) 70–79.
[54] J. Wang, Z. He, X. Tan, T. Wang, L. Liu, X. He, X.D. Liu, L. Zhang, K. Du, High-performance 2.6 V aqueous symmetric supercapacitor based on porous boron-doped diamond via regrowth of diamond nanoparticles, Carbon 160 (2020) 71–79.
[55] S. Zheng, Z.-S. Wu, F. Zhou, X. Wang, J. Ma, C. Liu, Y.-B. He, X. Bao, All-solid-state planar integrated lithium ion micro-batteries with extraordinary flexibility and high-temperature performance, Nano Energy 51 (2018) 613–620.
[56] G. Sun, J. An, C.K. Chua, H. Pang, J. Zhang, P. Chen, Layer-by-layer printing of laminated graphene-based interdigitated microelectrodes for flexible planar micro-supercapacitors, Electrochem. Commun. 51 (2015) 33–36.
[57] X. Shi, S. Pei, F. Zhou, W. Ren, H.-M. Cheng, Z.-S. Wu, X. Bao, Ultrahigh-voltage integrated micro-supercapacitors with designable shapes and superior flexibility, Energy Environ. Sci. 12 (2019) 1534–1541.
[58] Z. Liu, Z.-S. Wu, S. Yang, R. Dong, X. Feng, K. Müllen, Ultraflexible in-plane micro-supercapacitors by direct printing of solution-processable electrochemically exfoliated graphene, Adv. Mater. 28 (2016) 2217–2222.
[59] S.S. Delekta, A.D. Smith, J. Li, M. Östling, Inkjet printed highly transparent and flexible graphene micro-supercapacitors, Nanoscale 9 (2017) 6998–7005.
[60] W. Liu, C. Lu, H. Li, R.Y. Tay, L. Sun, X. Wang, W.L. Chow, X. Wang, B.K. Tay, Z. Chen, J. Yan, K. Feng, G. Lui, R. Tjandra, L. Rasenthiram, G. Chiu, A. Yu, Paper-based all-solid-state flexible micro-supercapacitors with ultra-high rate and rapid frequency response capabilities, J. Mater. Chem. 4 (2016) 3754–3764.
[61] H.Y. Li, Y. Hou, F.X. Wang, M.R. Lohe, X.D. Zhuang, L. Niu, X.L. Feng, Flexible All-solid-state supercapacitors with high volumetric capacitances boosted by solution processable MXene and electrochemically exfoliated graphene, Adv. Energy Mater. 7 (2017) 1601847.